Wadi Alshatti University Journal of
Pure and Applied Sciences

مجلة جامعة وادي الشاطئ
للعلوم البحتة والتطبيقية

Volume 3, No. 2, July-December 2025 Online ISSN: 3006-0877 المجلد 3، الاصدار 2، يوليو-ديسمبر 2025

RESEARCH ARTICLE HEAT TRANSFER

Numerical Solution of Natural Convection in Vertical Channels

Ahmed Habeb[1]*, Ahmed Alashlam[2]

[1]Faculty of Science, Aljufra University - Libya
[2] Faculty of Natural Resources, Aljufra University - Libya

ARTICLE HISTORY

Received 20 June 2025
Revised 18 July 2025
Accepted 21 July 2025
Online 22 July 2025

KEYWORDS

Natural convection;
Numerical solution;
Vertical channels.

ABSTRACT

A numerical study was conducted on a large vertical channel simulating passive solar air collector. The k–T turbulence model, implemented using the PHOENICS software, was applied to a vertical channel measuring 1 m in height and 1 m in width. The channel was heated from one side by a uniform heat flux (UHF), representing the absorber plate, while the opposite side (glazing) remained unheated. Different heat inputs (Q_{in}) and various aspect ratios (s/H) were tested. The governing equations, including turbulence transport equations, were solved using the finite volume method. Velocity profiles were determined to monitor the hydraulic development of airflow along the channel. Results showed that the average velocity increased with decreasing aspect ratio, while the mass flow rate increased with increasing aspect ratio. The Nusselt number - Nu(s) - and the Reynolds number - Re(s) - were used as the dimensionless heat transfer and air flow rate respectively were correlated against two independent variables, the modified Rayleigh number - Ra^* - and aspect ratio - s/H. Various empirical correlations were derived of the airflow and heat transfer rate represented by Nu(s) and Re(s) respectively. Numerical results were validated against previous experimental data from the literature, showing good agreement.

الحل العددي للحمل الحرفي القنوات العمودية

أحمد حبيب[1]*، أحمد الأشلم[1]

الكلمات المفتاحية

الحمل الحر
الحل العددي
القنوات العمودية

الملخص

أجريت دراسة عددية على قناة رأسية كبيرة تحاكي مجمّع هواء شمسي سلبي. تم تطبيق النموذج المضطراب k-T باستخدام برنامج PHOENICS على قناة رأسية يبلغ ارتفاعها 1 متر وعرضها 1 متر. تم تسخين القناة من جانب واحد باستخدام تدفق حراري منتظم (UHF)، يُمثّل صفيحة الامتصاص، بينما بقي الجانب المقابل (الزجاج) غير مسخن. تم اختبار مدخلات حرارية مختلفة (Q_{in}) ونسب أبعاد متنوعة (s/H). تم حل المعادلات الحاكمة، بما في ذلك معادلات الإنتقال المضطرب، باستخدام طريقة الحجوم المحدود. تم تحديد مخططات السرعة لمراقبة التطور الهيدروليكي لتدفق الهواء على طول القناة. أظهرت النتائج أن متوسط السرعة يزداد مع انخفاض نسبة الأبعاد، بينما يزداد معدل تدفق الكتلي مع زيادة نسبة الأبعاد. استُخدم عدد نوسلت ((Nu(s)) وعدد رينولدز ((Re(s)) لربط معدل انتقال الحرارة الأبعادية ومعدل تدفق الهواء، على التوالي، بمتغيرين مستقلين، هما عدد رايلي المعدل (Ra^*) ونسبة العرض إلى الارتفاع (s/H) . تم اشتقاق علاقات تجريبية متعددة لتمثيل تدفق الهواء ومعدل انتقال الحرارة عبر كل من Nu(s) و Re(s). تم التحقق من صحة النتائج العددية من خلال مقارنتها مع بيانات تجريبية سابقة من المراجع ، وأظهرت توافقًا جيدًا

Introduction

Passive solar systems have been an attractive area of interest because of their contributions in reducing the mechanical cooling and heating loads of modern buildings. These systems encompass solar walls (including Trombe walls), double-skin façades, solar chimneys, solar atria, and hybrid photovoltaic-thermal (PVT) façades. These all rely on buoyancy-driven (natural) convection to induce airflow, indicating that they are not dependent on any external mechanical aids (such as fans) to induce air movement or to enhance system performance. The science of buoyancy-driven convection is complex and has been an attractive area of scientific interest. Thus, for several applications, it is difficult to predict their performance, especially in large-scale systems. For instance, in solar façades, the relationships between key variables are complex and not fully determined, such as the geometry (height, depth) and heat input on the one hand, and on the other hand, the outputs from the system, such as heat transfer, thermal efficiency and airflow rate.

On this topic, there have been numerous attempts by researchers to address the issue either experimentally, analytically, or numerically. For example, [1-4] carried out indoor experiments and derived dimensionless correlations describing airflow and heat transfer for large-scale vertical channels. Other researchers, including [5-8] have conducted theoretical and analytical studies aimed at reducing time and

---

*Corresponding author

https://doi.org/10.63318/waujpasv3i2_18

simplifying the prediction of airflow, friction coefficients, and related parameters in such systems. Although experimental studies provide reliable results that reflect actual systems, Computational Fluid Dynamics (CFD) modeling offers advantages in terms of time and cost. However, it requires experience and a solid understanding of the physical principles to avoid misleading outcomes. Therefore, numerical simulation techniques have also been widely applied to characterize airflow and heat transfer within such systems. For example, the early numerical work of [9] studied the airflow within the Trombe wall channel and used practical parameters found in the literature to simulate turbulent flow. A numerical simulation for laminar flow in the Trombe wall was also conducted using the finite element method on a tilted surface to enhance the thermal performance [10]. A numerical simulation of a solar chimney with heat recovery was conducted to enhance the flow rate and reduce the thermal buoyancy effect, as reported by [11]. As documented by [12], the RNG (k-ε) turbulence model was applied to predict the flow within the Trombe channel, and the results were validated against experimental data found in the literature.

There are two different heating modes applied, depending on the heat input source, in natural convection heat transfer studies: Uniform Heat Flux (UHF), where the wall heat flux is known, and Uniform Wall Temperature (UWT), where the wall temperature is known. Various studies have published a wide range of CFD simulation results using the k-T model and considered important aspects related to passive solar heater such as optimum spacing and radiation effects for UWT and UHF heating modes, as reported by [13-17]. A numerical study was conducted on parallel plate vertical channels, considering the effects of ambient temperature, radiation, absorptivity, and the emissivity of the channel material [18]. Temperature and velocity profiles were evaluated at different elevations along a 3 m vertical channel and derived correlations of heat transfer rates for UWT mode were presented by [19, 20]. Moreover, passive solar heating technology, which is based mainly on buoyancy-driven force and temperature difference, can also play a natural role in cooling the solar photovoltaic panels. Solar panels should be installed a few centimetres away from the roof of the building or other parallel surface (flat plate air collector) to create an air current behind the panel to allow a natural cooling process that helps maintains the solar PV at a higher efficiency level. Based on this concept, [21-25] carried out various types of investigations in order to minimize the temperature of PV surface to enhance their performance and efficiency. On small-scale channels, [26, 27] conducted an extensive experimental work on inclined channel varied from 30° to 90°. Correlations under the UHF heating mode were derived for evaluating the airflow and heat transfer rate.

Studies concerning airflow and heat transfer under the UHF heating mode for large scaled vertical channels are countable. The only published experimental that are comparable with the present work are for [1-3] considering the UHF mode for a big scale vertical channel. Therefore and in order to develop a CFD model, the present study is based on a numerical solution of airflow in a large-scale vertical channel simulating a thermosyphoning air panel or solar chimney. The k-T turbulence model was the only model used in the current study, as it is considered reliable for transitional and low-Reynolds-number flows, particularly for calculating vertical velocities [28]. Two independent variables - Qin and s/H - were examined, and their effects were analyzed and presented in the form of dimensionless correlations. Validation of the current results against available data in the literature is proposed. The outcome of the current project may help engineers and designers to evaluate the thermal and the hydraulic performance of such actual solar collectors.

The Physical Model

A typical single-pass passive solar air heater is incorporated into the building facade where the solar radiation is trapped between the heated surface (plate) and the cover (glazing), heating the air and delivering it into the living space. Figure 1 shows the model dimensions and specifications, which include two vertical walls simulating the absorber (heated surface) and the cover (glazing). The absorber is made of a black painted aluminum sheet and insulated by thermal insulation, while the glazing is made of clear glass - all components together simulate a passive solar air heater. The size of the model is about 1m^2, represented by the area of heated plate. Different values of the heat inputs and different channel depths were tested to derive correlations describing the thermal and hydraulic performance of such systems. The model had closed sides and was open at top and bottom.

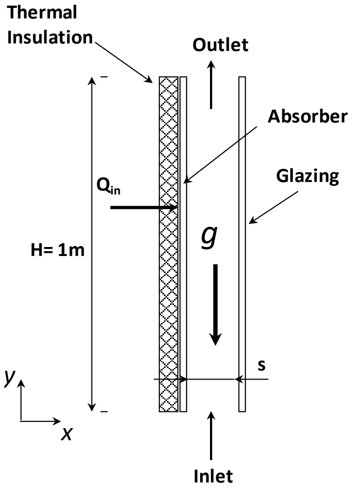

Fig. 1: Scheme of a Two Dimensional Vertical Channel

Numerical Simulation

In fluid mechanics problems, computational fluid dynamics (CFD) techniques are used to solve complex partial differential equations governing fluid flow. The zone under study is divided into a grid or mesh of small cells or volumes, and by using established relationships for flow within and between them, the overall flow pattern can be determined: round obstacles, through ducts, etc. The validity of solutions depends, not only on the correct mathematical underlying relationships, but also on the mesh size and the boundary conditions that apply to the problem. The CFD technique has been widely used for large and strategic projects such as in aerospace and commercial projects, i.e. internal combustion engines and turbines [29]. With the rapid development of computer technology, there have been many CFD codes developed and now available worldwide. The CFD software used in this project is PHOENICS, which stands for Parabolic Hyperbolic Or Elliptic Numerical - Integration Code Series and was developed by [30, 31]. PHOENICS is designed to solve problems in single-phase or two-phase flow, heat transfer, chemical reactions operations and other problems related to environmental science. The software is capable of simulating flow whether it is steady or unsteady and whether it is laminar, transitional or turbulent. The code also contains various turbulence models, such as the k-γ and k-ω models that can deal with convective heat transfer problems. The governing equations, conservation of mass, momentum, energy and other related model equations, are solved by a finite volume method. Modeling of laminar flow has been greatly developed and is relatively straightforward compared with turbulent flow. One of the simplifying features of steady-state laminar flow is that changes in the flow pattern or other disturbances, such as eddies, are not expected. Excellent results can be obtained, especially if the gird is well resolved and the boundary is specified correctly. For flow in a vertical duct, a two-dimensional model can be assumed. Simulating or modeling of turbulent flow is more difficult because, even in steady-state conditions, it is still affected by random internal turbulence. This unsteadiness comes naturally from the behavior of different sizes of eddies that act in different directions and in chaotic manners. To simplify the solution of the turbulent flow problem, extra equations or models are required to complete the task. The model used in this study is the k-ω model developed by [32, 33], which enhances the low-Reynolds number effects, for example, compressibility and shear effects. The standard model is based on an experimental model and with transport equations for the kinetic energy (k) and turbulence parameter (ω).

The Continuity Equation

$$\frac{\partial(\rho u)}{\partial x}+\frac{\partial(\rho v)}{\partial y}=0 \tag{1}$$

X: Momentum Equation

$$\rho u\frac{\partial u}{\partial x}+\rho v\frac{\partial u}{\partial y}=-\frac{\partial p_m}{\partial x}+\frac{\partial}{\partial y}\left[(\mu+\mu_t)\frac{\partial u}{\partial y}\right]+\frac{\partial}{\partial x}\left[(\mu+\mu_t)\frac{\partial u}{\partial x}\right] \tag{2}$$

Y: Momentum Equation

$$\rho u\frac{\partial v}{\partial x}+\rho v\frac{\partial v}{\partial y}=-\frac{\partial p_m}{\partial y}+(\rho_m-\rho)g+\frac{\partial}{\partial y} \tag{3}$$

Energy Equations

$$c_p\rho u\frac{\partial T}{\partial x}+c_p\rho v\frac{\partial T}{\partial y}=\frac{\partial}{\partial y}\left[(k+\frac{c_p\mu_t}{\sigma_t})\frac{\partial T}{\partial y}\right]+\frac{\partial}{\partial x}\left[(k+\frac{c_p\mu_t}{\sigma_t})\frac{\partial T}{\partial x}\right] \tag{4}$$

k-ω Turbulent Model Equations

Transport Equation for Kinetic Turbulence Energy k

$$\frac{\partial}{\partial t}(\rho k)+\frac{\partial}{\partial x_i}(\rho k u_i)=\frac{\partial}{\partial x_i}\left[\left(\mu+\frac{\mu_t}{\sigma_k}\right)\frac{\partial k}{\partial x_i}\right]+G_k-Y_k+S_k \tag{5}$$

Transport Equation for Turbulence Frequency ω

$$\frac{\partial}{\partial x_i}\left[\left(\mu+\frac{\mu_t}{\sigma_k}\right)\frac{\partial k}{\partial x_i}\right]+G_k-Y_k+S_k$$

$$\frac{\partial}{\partial t}(\rho\omega)+\frac{\partial}{\partial x_i}(\rho\omega u_i)=\frac{\partial}{\partial x_i}\left[\left(\mu+\frac{\mu_t}{\sigma_\omega}\right)\frac{\partial \omega}{\partial x_i}\right]+G_\omega-Y_\omega+S_\omega \tag{6}$$

General Transport Equation applied in PHOENICS in Cartesian 2D format is:

$$\frac{\partial}{\partial t}(\rho\phi)+\frac{\partial}{\partial x}(\rho u\phi)+\frac{\partial}{\partial y}(\rho v\phi)=\frac{\partial}{\partial x}\left(\Gamma_\phi\frac{\partial\phi}{\partial x}\right)+\frac{\partial}{\partial y}\left(\Gamma_\phi\frac{\partial\phi}{\partial y}\right)+S_\phi \tag{7}$$

The first term is known as transient, the second and the third are known as convective, the fourth and the fifth are diffusive, and the sixth is source. ϶N is the exchange coefficient variable. More details can be found in [28, 32, 33]. It is impossible to reach an analytical solution for the transport equations, and so numerical techniques are used. The partial differential equations are converted into algebraic equations to include the unknown values of temperature and pressure and other variables at discrete points within the domain. If the number of these discrete points in the computation domain and iterations is infinitely large, then the solution would be exactly within the limit of the equations used in the model, but practical limitations of discretization mean that rounding and other errors will occur. There are several methods available to solve the partial differential equations, and PHOENICS uses finite volume discretization in which the computational domain is subdivided into volumes (3-D case) or cells (2-D case). The general transport equation is integrated over each volume or cell with the assumption of a profile within the volume or cell for each variable [34].

Boundary Conditions and Grid Generations:

The biggest challenge encountered here was to set up accurate boundary conditions for the model, particularly the inlet and the outlet of the channel, where specifying, for example, the correct pressure and temperature values may sometimes be dissimilar to the actual situation. After some initial runs, it became clear that the size of the computational domain, boundary conditions, and mesh size all had an impact on the simulation results. Thus, the main domain was recommended to be significantly larger than the vertical channel itself, first to ensure solutions with fewer errors, and second, to introduce the effect of the ambient conditions into the calculation, which leads to a better picture of the inlet and the outlet of the channel model (pressure and temperature). The Immersol radiation model, part of the PHOENICS suite, was activated only to obtain results close to the actual situation, and, therefore, emissivity and other radiation properties for various components were estimated according to the PHOENICS library data, but no further considerations were taken into account regarding the radiation effect for calculation and deeper analysis. The boundary conditions of the problem can be addressed as follows (see Figure 2):

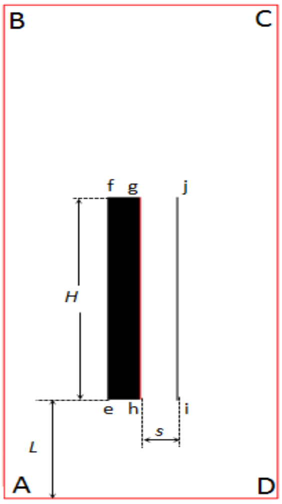

Fig. 2: Scheme of Computational Domain

- Main domain ABCD: AB = CD = 2.5m, AD=BC=1m.
- Heated plate(gh) (height H=1 m, emissivity ε=0.86) was placed at L=0.5m away from the bottom of the domain.
- Thermal insulation (ε=0.86) efgh made of phenolic foam with a thermal conductivity of 0.018W/mK.
- The cover (ij) is made of clear glass (ε=0.92) with a height H; thermal conductivity of 1.39 W/mK and assumed to be adiabatic.
- Channel entrance (hi) as well as channel exit (gj) was kept to the surrounding condition of the main domain ABCD to provide better details about the two regions close to the actual condition.
- No-slip boundary conditions were assumed at the surfaces.
- Uniform heat flux (UHF) at the heated plate, $q=k(\partial T/\partial n)$, where n is the coordinate perpendicular to the plate.
- AB, BC, CD and DA are assumed to have fixed pressure boundaries (P=0), fixed temperature equal to ambient and zero velocity ($u = v = 0$).
- The initial condition of each run was set up for the ambient temperature and ambient pressure.
- Other assumptions and constant values of the boundary condition are generated automatically by the software library (more details can be found in [28].

As stated earlier, the final choice for the domain size was x=1 m, y=2.5 m, and z=1 m; whereas the size of the model simulating the channel was x=(variable channel depths), y=1 m, and z=1 m (a 2D model with one-cell thickness in the z direction) (see Figure 3). Several structured, non-uniform cartesian grids and arrangements for the model were tested. The power law distributions were applied to achieve a fine grid near boundaries (region of interest). The final grid definition is shown in Figure 3 with finer grid spacing at boundaries and other areas of interest (surfaces, inlet, and outlet of the duct, etc.), which remained constant for all channel depths and heat inputs. Several grid testing attempts were performed in order to determine the size, number, and type of the mesh. The purpose of this was to set up a mesh that achieves the convergence of the solutions more easily. A grid independence test was also conducted on the numerical solution considering the k–T model. Power-law grid generation was applied in both directions (see Appendix 1 for uncertainty analysis). The final grid proposed here - see Figure 3 - for the main channel contains a non-uniform cartesian grid which had vertically 75 cells of 1.15 power ratio (finer at the inlet and outlet) and 52 cells of 1.1 power ratio (finer at the heated wall and the glazing).

Model Run and Data Collection

Only two pieces of information were used to initiate the CFD modeling, namely the ambient temperature (25°C), the heat input (200W to 1000W, 5 sets tested - at 200W intervals), and the desired channel depths (45mm to 145mm, 6 sets tested - at 20mm intervals). A laminar model was initially used to solve the governing equations, but it did not yield the desired results. Therefore, a turbulence model was recommended instead. The governing equations were then solved using the k-ω model because it includes a low-Reynolds extension for near-wall turbulence, as stated in [28]. The k-ω turbulence model solves the transport equations for the turbulent kinetic energy k and the turbulence frequency ω. The model has several variations, and the PHOENICS-adopted model is based on [32, 33] The k-ω model is not as popular as the k-ε model, for example, but has several advantages. It is very stable, particularly for the low-Re version, as it converges faster than the k-ε model, and it is more economical because it does not require the calculation of wall distance, as stated in [28]. In addition, there is one possible reason for not using the k-ε model is that the validity of the wall function method is applicable to forced-convection flows, but not strictly for natural convection boundary layers. Although solutions to natural convection problems are not easy to obtain, 12,000 iterations were sufficient to reach convergence in all cases. Convergence was declared as the normalized residuals for the mass, momentum, energy, and turbulent variables became less than 10^{-4}. A converging solution occurs when the changes in solved values become smaller with each iteration and can finally be negligible. The converging process for all variables is tracked by the software main screen (Figure 4) where the curves in the spot values become horizontal, proving that the changes are very small. In addition, the curves on the right, representing the logarithms of the sums of the absolute residuals, fall down to the default values of the relevant relaxation parameters, and this can be checked in the Result file.

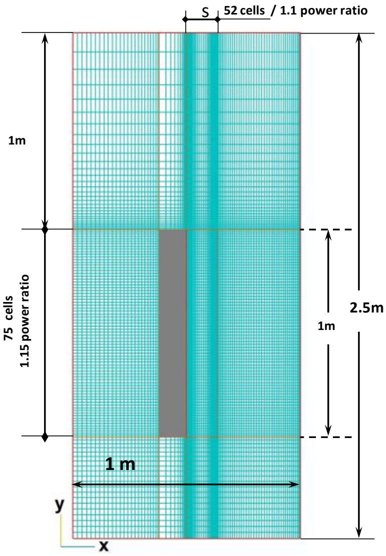

Fig. 3: Computational Domain Grid Distributionn

Data Analysis and Discussions

This section examines the output results from the CFD simulations for the system in steady state condition. This includes only the hydraulic performance of the system at which the calculated velocities and the mass flow rate and other related parameters are considered and analyzed. Velocities at different elevations along the channel were computed and their profiles at the same locations were obtained to draw a picture of the hydraulic development along the channel. Results are shown in Figure 5, where the image (vectors and contour) clearly shows the velocity variations within the whole computational domain. It illustrates the airflow motion in the channel and surrounding. It can be observed that the highest velocity takes place at the hot surfaces (heated plate) and cover (glazing) where the warmer airflow exists and moves upwards. At the center of the channel, the airflow velocity is lower than at the two surfaces where the air is cooler. In addition, at the exit, the flow leaves the duct parallel to the surface and no reverse flow or eddies are detected.

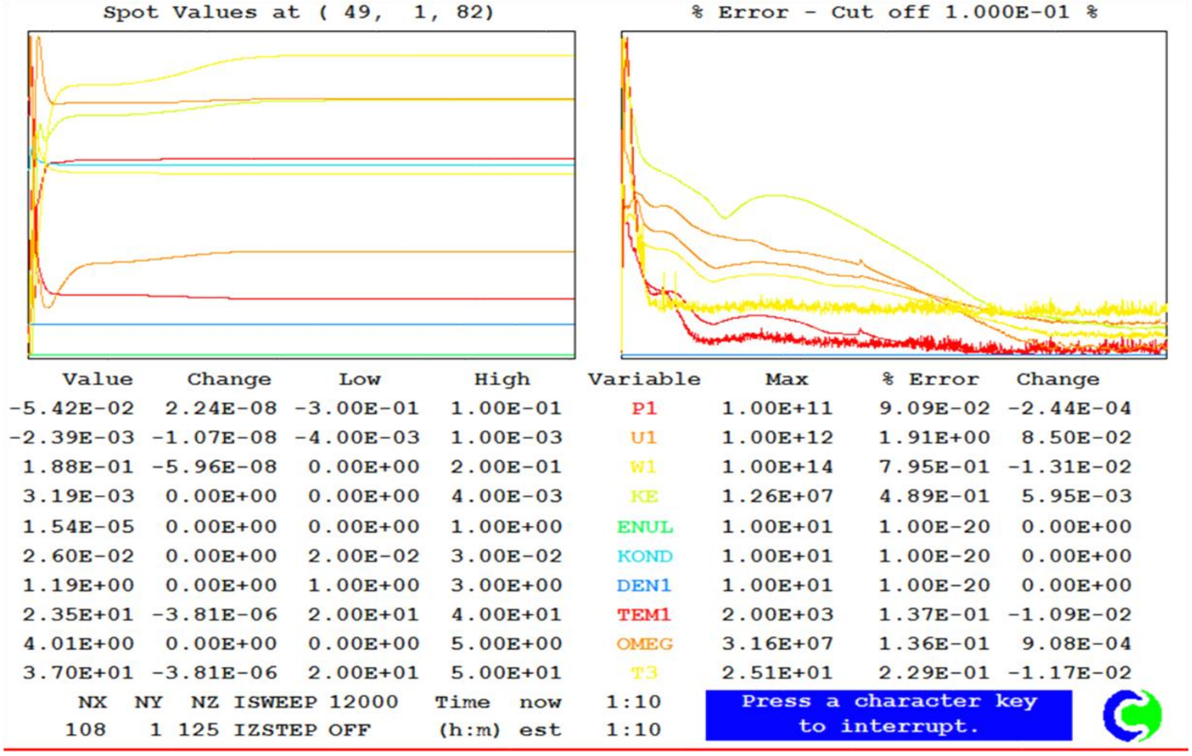

```
Spot Values at ( 49,   1, 82)                    % Error - Cut off 1.000E-01 %

   Value      Change       Low        High     Variable     Max       % Error    Change
-5.42E-02   2.24E-08  -3.00E-01   1.00E-01       P1      1.00E+11   9.09E-02  -2.44E-04
-2.39E-03  -1.07E-08  -4.00E-03   1.00E-03       U1      1.00E+12   1.91E+00   8.50E-02
 1.88E-01  -5.96E-08   0.00E+00   2.00E-01       W1      1.00E+14   7.95E-01  -1.31E-02
 3.19E-03   0.00E+00   0.00E+00   4.00E-03       KE      1.26E+07   4.89E-01   5.95E-03
 1.54E-05   0.00E+00   0.00E+00   1.00E+00      ENUL     1.00E+01   1.00E-20   0.00E+00
 2.60E-02   0.00E+00   2.00E-02   3.00E-02      KOND     1.00E+01   1.00E-20   0.00E+00
 1.19E+00   0.00E+00   1.00E+00   3.00E+00      DEN1     1.00E+01   1.00E-20   0.00E+00
 2.35E+01  -3.81E-06   2.00E+01   4.00E+01      TEM1     2.00E+03   1.37E-01  -1.09E-02
 4.01E+00   0.00E+00   0.00E+00   5.00E+00      OMEG     3.16E+07   1.36E-01   9.08E-04
 3.70E+01  -3.81E-06   2.00E+01   5.00E+01       T3      2.51E+01   2.29E-01  -1.17E-02
      NX   NY   NZ ISWEEP 12000   Time   now    1:10    Press a character key
     108    1  125 IZSTEP OFF    (h:m)  est    1:10       to interrupt.
```

Fig. 4: Convergence Monitor

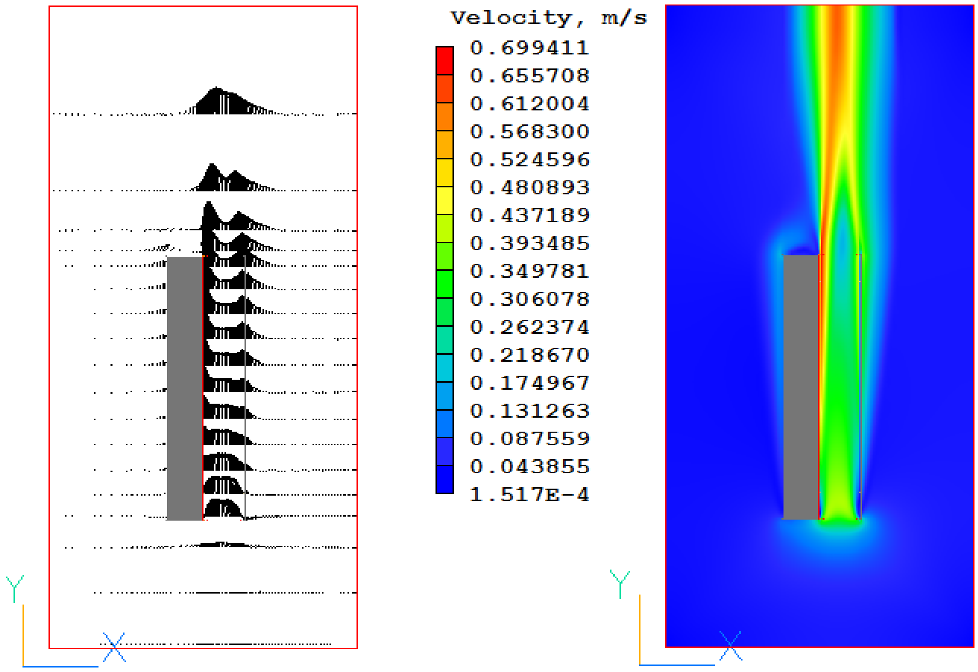

Fig. 5: Flow Vectors and Contours (105mm - 800W)

Velocity Profiles

The velocity profiles were also obtained using PHOENICS code, both at bottom and top. Figs. 6a and 6b show examples of the velocity profiles taken at the bottom/entrance of the channel, at y/H=0.0 for 45mm and 105mm channel depth and all values of heat inputs. Whilst these profiles are mostly flat across the entrance of the channel, at wider channel depths (channel depth 105mm) the profiles show two modest peaks at the walls and lower velocity at the center of the channel. The velocity profiles were also calculated at the top of the channel for all cases and the 45mm and 105mm channel depths are shown in Figure 7a and 7b as an example to demonstrate the effect of the heat input and the channel depth on the shape of the velocity profiles. The velocity is higher at the heated plate than at the cover and less in between. For the smaller channel depths, the profile is almost a straight line between the plate and cover, whereas, for the wider channel depth, there is a distinct dip between two peaks. At the bottom of the channel and at the top the dominant velocity component is the vertical. Similar qualitative observations were made by [19, 20, 35].

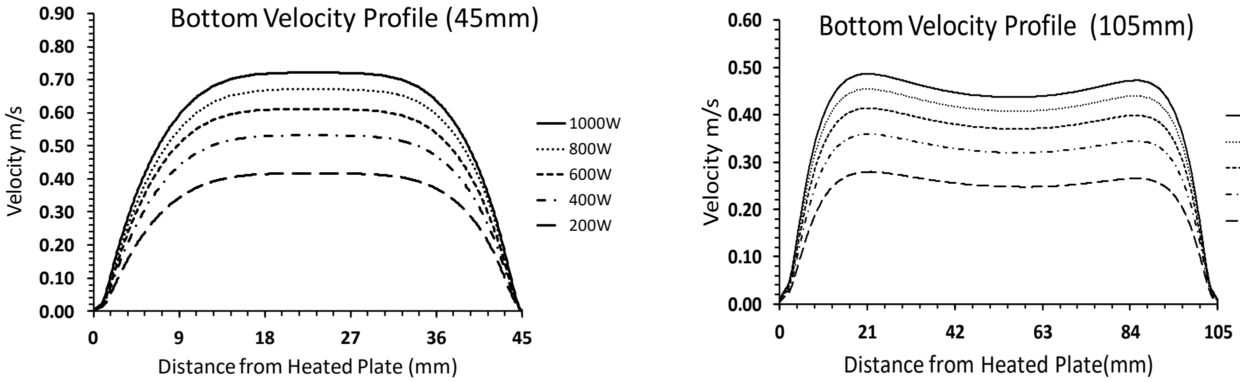

(a) 45mm Channel depth **(b)** 105mm Channel depth

Fig. 6: Bottom Velocity Profile

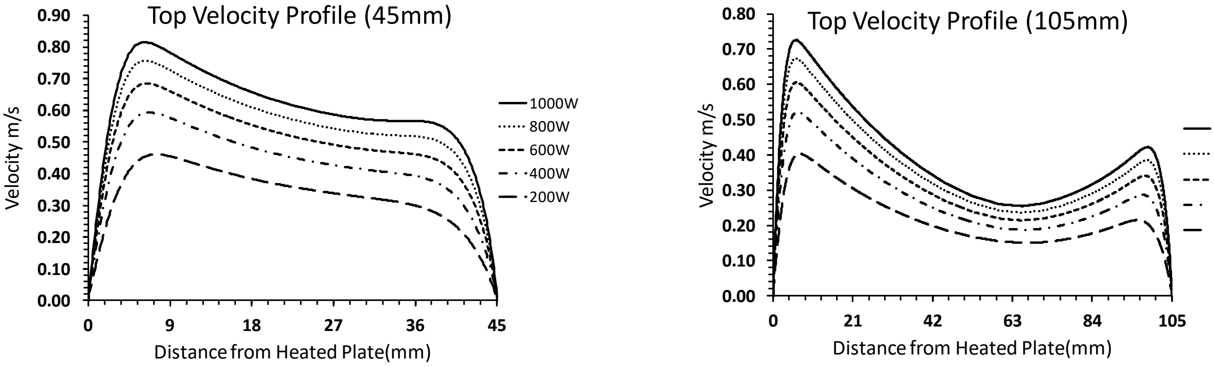

(a) 45mm Channel depth **(b)** 105mm Channel depth

Fig. 7: Top Velocity Profiles

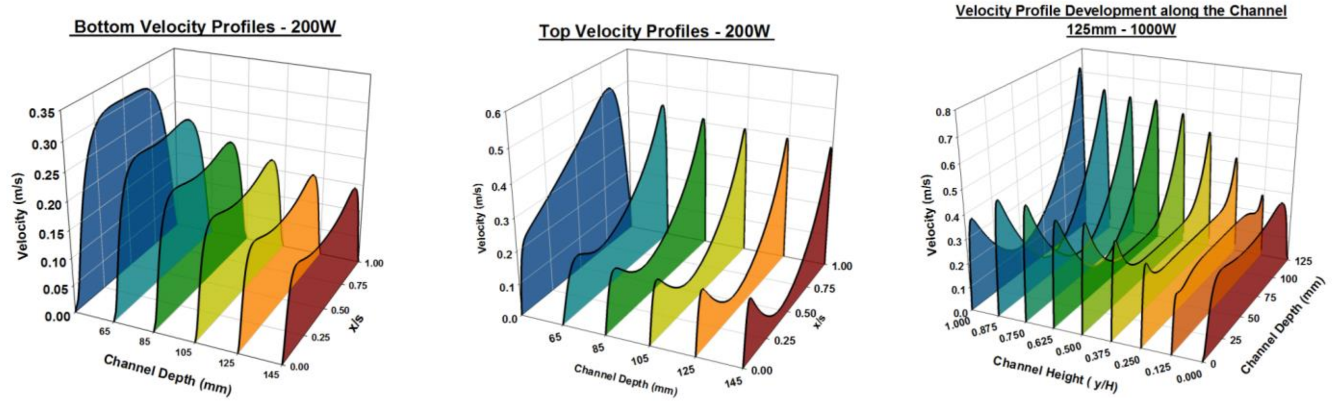

(a) Bottom Velocity Profiles at y/H=0 **(b)** Top velocity Profiles at y/H=1.0 **(c)** Variations of Velocity Profiles

Fig. 8: Variations and Developments of Velocity Profiles

One of the advantages of CFD modeling is that it can provide data for any part of the computational domain and offers any desired details at different locations. Therefore and with the help of the SigmaPlot software package, Figures. 8a and 8b show how the velocity profiles at the bottom and top of the channel, respectively, vary with channel depth at the same heat input. It is clear that the velocity profiles and their shape are affected very much by the channel depths due to distance between the two surfaces. Figure 8c also shows the development of the velocity profiles at different elevations along the length (height) of the channel, from a flat, undeveloped profile at entrance to a very 'peaky' profile at exit. Qualitative observations were also noticed by [19, 20, 35].

Average Velocity and Mass Flow Rate

Calculated average velocities based on entrance conditions were also accomplished. It was found that the average velocity (Figure 9a) is a function of the heat input and the channel depth increases as the channel depth decreases and the heat input increases, in line with findings by [1, 2] However, calculated mass flow rates (Figure 9b) were found to increase as the heat input and the channel depth increase. The rate of increase slows down as the heat input decreases and the channel depth decreases. Similar findings were achieved by, for example [6], whose calculated mass flow rate agrees well with their experimental data.

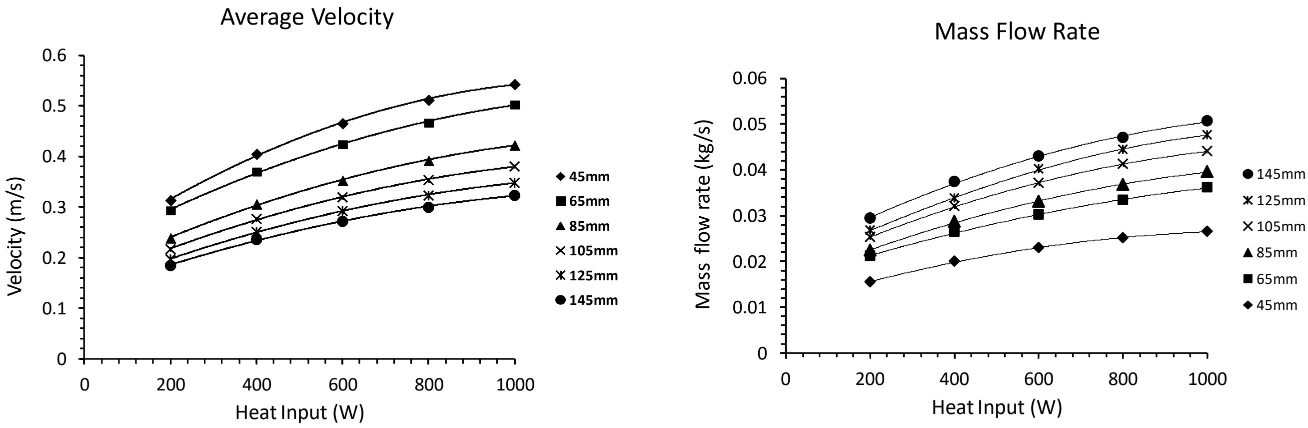

(a) Computed Average Velocity **(b)** Computed Mass Flow Rate

Fig. 9: Average Airflow Velocities and Mass Flow Rate

A reverse flow was observed at a channel depth of 0.30 m [4, 36] but no reverse flow was observed, nor was an optimum channel depth identified in the present study.

Airflow Dimensionless Correlations

In order to complete the description of hydraulic behaviour due to buoyancy-driven convective heat transfer, relevant correlations between dimensionless groups, such as Nusselt number (Nu), Reynolds number (Re) and Rayleigh number (Ra*), are correlated using the least square method and multiple regression procedure. The purpose of this is to investigate the effect of heat input (Qin) indirectly accommodated by Ra* and the channel depth (s) indirectly represented by s/H on the performance of the system. Ra*, as proposed by [37], is more appropriate for UHF problems because it is evaluated according to a known and constant heat flux, whereas the usual form of Rayleigh number is based on a temperature difference, which is suitable for the UWT cases. The procedure technique, presented here, is followed by, for example, [1, 2, 3].

The main parameters used here are:

Modified Rayleigh number

$$\mathrm{Ra}^* = \frac{g\,\beta\,q_c\;H^4}{k_m \nu^2{}_m}\;\mathrm{Pr} \qquad (8)$$

Reynolds number

$$\mathrm{Re}(s) = \frac{\bar{u}_i\,s}{\nu_i} \qquad (9)$$

Nusselt number, Nu(s), based on the channel depth (s):

$$\mathrm{Nu}(s) = \frac{\bar{h}\,s}{k_m} \qquad (10)$$

Where:

Mass Airflow rate (kg/s): $\dot{m} = \rho_i\,A_c\,\bar{u}_i$

Convective heat to the airflow (W): $Q_c = \dot{m}\,c_p\,(T_o - T_i)$

Mean heat transfer coefficient (W/m^2°C): $\bar{h} = \frac{Q_c}{A_p\,(T_p - T_m)}$

For the rectangular cross-section used in this study, D_h varies between 1.75 and 1.91 times the channel depth s. Therefore, the Reynolds number, Re(D_h), based on the hydraulic diameter (D_h), is almost double Re(s). The Reynolds number is considered as an indicator of the flow regime in forced convection and the Rayleigh number for buoyancy-driven convection. However, for buoyancy-driven convection in ducts where the flow is constrained, the Reynolds number is often used as a non-dimensional flow parameter, but it is sometimes used to determine friction factors, as noted by [6]. In addition, it is utilized as a dimensionless expression of air velocity since no other expression can play the role; [1-3]. Since the current study is based on the effect of the channel depth (s) and heat input (Qin), Reynolds number based on the channel depth, Re(s) is applied here.

Nusselt Number Variations

CFD simulation outcomes show that Nu(s) - dimensionless correlation coefficient based on channel depth (s) - is considered here, correlated against Ra*. Figures 10 shows that Log (Nu(s)) increase as the Log Ra* and channel depth increases.

The mathematical form was assumed to take the following form:

$$Nu(s) = a(Ra^*)^b(s/H)^c \qquad (11)$$

The regression analysis procedure was carried out and empirical coefficients ***a, b*** and ***c*** are listed in Tables 1 along with the results of [1, 3] comparison including the standard error (S.E) and the correlation coefficient (R^2).

Table 1: Regression Coefficients for Nu(s) against Ra*

Constant	***a***	***b***	***c***	**S.E**	**R^2**
Current Results, H= 1m	0.225	0.215	0.503	0.0058	0.996
La Pica et al [1] , H= 2.6m	0.577	0.203	0.895	0.0230	0.980
Ryan[3] H=1.025m	0.014	0.346	0.973	0.0247	0.993

For comparison and according to Table 1, there are similarities between the current results and the results of [1] particularly the exponent b which is closed to 0.25 - denoted as the traditional exponent in natural convection, [38], despite the difference in heights and inlet and outlet geometry and the cover that was aluminized to reduce radiation losses to a minimum. [3] used a test rigs similar in size to the current model, but the inlet temperature was measured approximately 50mm above the true level of the inlet, which might have affected the recorded ‘inlet temperature’ data and hence also the derived results. As just stated, [38] quoted 0.25 for the constant b, which is the rate of heat transfer from the heat surface to the airflow. Therefore, Figure 11 shows N(s)Ra*-0.25 plotted against s/H which presents good correlation and little scatter, where the constant 'c' was initially close to 0.25. Therefore, these results confirm that heat transfer coefficient is proportional to fourth root of the heat gain.

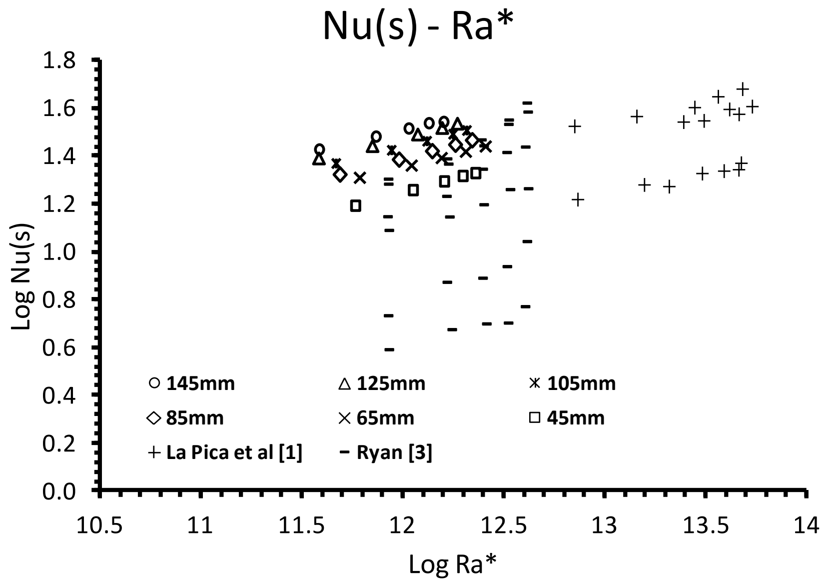

Fig. 10: Nu(s) Variation with Ra*

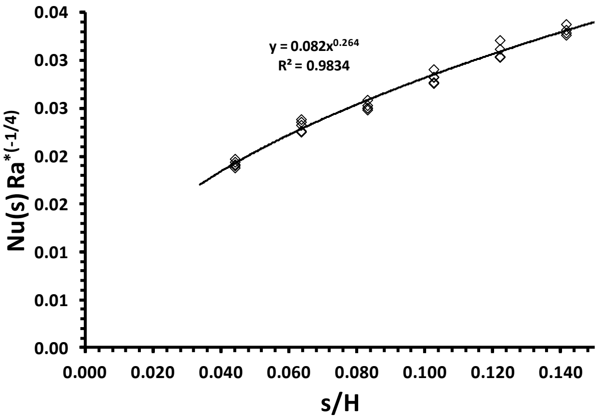

Fig. 11: Heat Transfer Dependence on Channel Depth

Reynolds Number Variations:

The Reynolds number - Re(s) - based on the channel depth - s -, Log(Re(s)), is plotted in Figure 12 against Log(Ra*), as it can be clearly seen that Log(Re(s)) increases linearly as both the channel depth and Ra* (the heat input) increase in all cases.

The mathematical form was assumed to take the following form:

$$Re(s) = a(Ra^{*})^{b}(s/H)^{c} \qquad (12)$$

The regression analysis procedure was carried out and empirical coefficients ***a, b*** and ***c*** are listed in Tables 2 along with the results of La Pica et al. (1993) and Burek and Habeb (2007) for comparison including the standard error (S.E) and the correlation coefficient (R^2).

The regression analysis procedure was carried out and empirical coefficients a, b and c are listed in Tables 2 along with the results of [1, 2] for comparison including the standard error (S.E) and the correlation coefficient (R^2). According to Table 2, the constant are quite close. The differences can be attributed to variations in geometry, experimental setup, or operating conditions. The channel used by [1] had an area of approximately 3 m², with channel depths of 7.5 cm, 12.5 cm, and 17 cm, and a heat input ranging from 48 to 317 W/m. . Burek and Habeb [2] employed a similar channel size and heat input values, but the range of channel depths tested was different (20 cm to 110 cm). These differences are sufficient and reasonable to explain the small variations and scatters observed in the present results and their corresponding correlations.

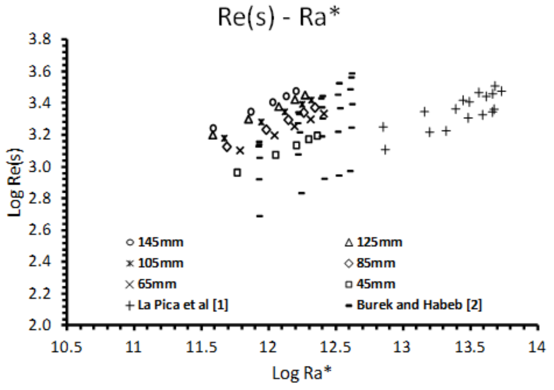

Fig. 12: Re(s) Variation with Ra*

Table 2: Regression Coefficients for Re(s) against Ra*

Constant	*a*	*b*	*c*	S.E	R²
Current Results, H= 1m	0.275	0.364	0.627	0.0063	0.998
La Pica et al [1] H= 2.6m	3.508	0.315	0.421	0.0106	0.992
Burek and Habeb [2] H=1.025m	0.00116	0.572	0.712	0.046	0.994

A theoretical expression was derived by [39], showing that mass flow rate and velocity are proportional to the cube root ("1" /"3") of the heat gain, in the absence of friction. However, their experimental data gave the value of the exponent 0.43 for both open-ended channels, and they attributed the difference to the experimental difficulties. The current CFD results were examined using the following correlation:

$$\mathrm{Re(s)Ra}*^{-1/3} = \mathrm{a}\ (\mathrm{s/H})^{\mathrm{c}} \qquad (13)$$

The results are presented in Figure 13. The data points show little scatter, and therefore the lumped-parameter model can be regarded as a good representation. For all sets of data, the dependency of flow rate on the depth-to-height aspect ratio (s/H) is close to 0.6:

$$\dot{m} \propto (s/H)^{0.6} \tag{14}$$

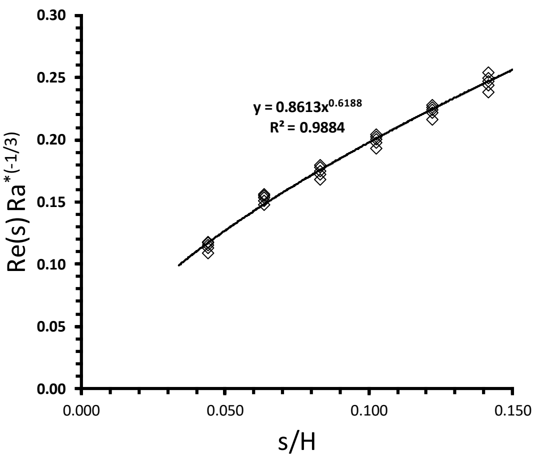

Fig. 13: Flow Rate Dependence on Channel Depth

Nusselt Number Variations with Reynolds

In order to investigate the relationship between heat transfer coefficient and velocity, LogNu(s) is plotted against LogRe(s). Figure 14 shows Log Nu(s) increases linearly as Log(Re(s)). The regression results yield the following correlation:

$$\mathrm{Nu}(s) = 0.136\ \mathrm{Re}^{0.693} \tag{15}$$

Table 3: Regression Coefficients for Nu(s) against Re(s)

Constant	*a*	*b*	S.E	R^2
Current Results	0.136	0.693	0.0104	0.987
Holman [40]	0.023	0.8	-	-

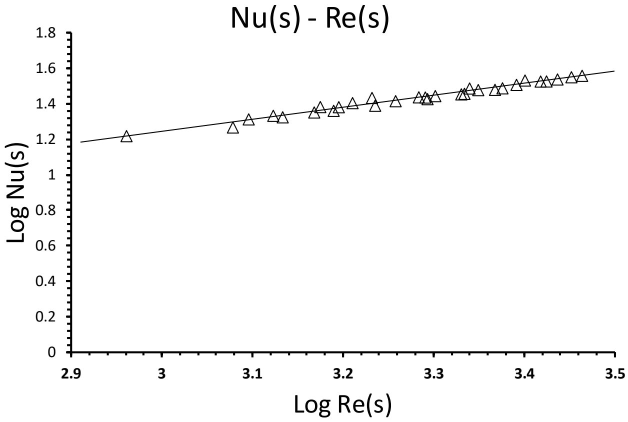

Fig. 14: Nu(s) against Re(s)

Holman [40] presented an empirical formula characterizing heat transfer rate, Nu, as a function of Re and Pr for a forced - convection fully developed flow inside a horizontal smooth tube under UHF mode and varied Prandtl number (from 0.6 to 100). See equation (16).

$$\mathrm{Nu}(s) = 0.023\ \mathrm{Re}(s)^{0.8}\ \ \mathrm{Pr}^{0.4} \tag{16}$$

According to Table 3 Although there are some similarities between the outcome of equation 15 and equation 16, the latter cannot be applied here as it was based on a wide range of Prandtl numbers (from 0.6 to 100) and derived from a forced - convection fully developed flow in a fixed circular - cross-section horizontal duct (tube).

Therefore, further investigation should be carried in future studies in regard to this issue.

Conclusion

The current CFD study was carried out on a large scale vertical channel simulating a passive solar collector. The present numerical study has led to some important findings regarding the performance of airflow in such systems. Airflow was examined under different conditions and, under different parameters. It was found that the average velocity increased with decreasing aspect ratio, while the mass flow rate increased with increasing aspect ratio. No reverse flow was detected. Figure 9 shows that the rates of increase tend to level off, suggesting the existence of optimum channel depths. This supports the findings of [4, 40], who observed reverse flow in channels wider than 0.3m, indicating an optimum channel depth. According to Table 1 and 2, heat transfer coefficient, represented by Nu(s), is proportional to $Q_{in}^{0.215}$ and to $s^{0.503}$ and the airflow, represented by Re(s), is proportional to $Q_{in}^{0.364}$ and to $s^{0.627}$, respectively, since Ra* and s/H indirectly accommodate the heat input and the channel depth, respectively. These correlations help designers to evaluate the performance of these collectors in order to reduce time and cost. All derived correlations are applicable under the following conditions:

$$45\text{mm} \le s \le 145\text{mm}$$
$$200\text{W} \le Q_{in} \le 1000\text{W}$$
$$912.3 \le \mathrm{Re}(s) \le 2973.6$$
$$5.8\ 10^{11} \le \mathrm{Ra}^* \le 1.6\ 10^{12}$$

Future Work

It would be worthwhile to investigate a wider range of channel depths and several different heights. The aim is to determine the exact optimum channel configuration and to study the effect of various heights. Additionally, testing the ducted entrance and exit of the channel would be important to understand their impact on the system's performance. Finally, upgrading the current CFD model to include radiation heat transfer would further enhance the study.

Author Contributions: "All authors have made a substantial, direct, and intellectual contribution to the work and approved it for publication."

Funding: "This research received no external funding."

Conflicts of Interest: "The authors declare that they have no conflict of interest."

Acknowledgment: "Authors would gratefully thank the supporting team at CHAM for their positive feedback and consultation. My sincere appreciation to Dr Brian Spalding - Head of CHAM - who provided me with a free short-period PHOENICS license to complete the current work."

Nomenclature

a, b	Regression coefficients (see Equation 15).
A_C	Cross section area of the channel (s x w) m^2.
A_P	Hot plate Area ($1m^2$).
C_p	Specific heat at constant pressure, kJ/kg.K.
D_h	Hydraulic Diameter (m)
G	Acceleration due to gravity (= 9.81 m/s^2).
G_k	Generation of k equation 5.
G_ω	Generation of ω equation 6.
H	Convective heat transfer (W/m^2K).
H	Channel height = 1m.
K	Thermal conductivity of air (W/m.K).

K	Turbulent kinetic energy.
P	Pressure, N/m^2.
$\dot{m}$	Mass airflow rate (kg/s).
Pr	Prandtl number.
q_c	Convective heat to airstream (W/m^2).
Q_{in}	Heat Input (W/m^2).
Ra^*	Rayleigh number
Re(s)	Reynolds number based on channel depth
s	Channel depth (m).
S_k	Source term equation 5.
S_ω	Source term equation6.
S_ϕ	Source term equation7.
T_a	Ambient Temperature (°C)
T_i	Inlet mean temperature (°C).
T_m	Mean temperature (T_o+T_i/2 (°C)).
T_o	Outlet mean temperature (°C).
T_p	Hot plate mean temperature (°C).
u	Horizontal velocity component , m/s.
u_i	Air bulk velocity (m/s).
v	Vertical velocity component , m/s.
x	Horizontal direction.
y	Vertical direction.
Y_k	Dissipation of k, equation5.
Y_ω	Dissipation of ω, equation 6.
w	Channel width = 1m.

Greek symbols:

β	Expansion coefficient (1/K).
r	Dencity (kg/m^3).
Γ_ϕ	Exchange coefficient of variable, φ equation 7.
μ	Dynamic viscosity coefficient, N.s/m^2.
μ_t	Dynamic turbulent viscosity coefficient, N.s/m^2.
v	Kinematic viscosity (m^2/s).
ρ	Fluid density, kg/m^3.
ρ_m	Mean fluid density, kg/m^3.
σ_k	Prandtl number of k, =2, equation 5.
σ_ω	Prandtl number of ω, =2, equation 6.
σ_t	Turbulent Prandtl number, equation 4.
ϕ	Computer variable, equation7.
ω	Dissipation or turbulence frequency.

References

[1] A. La Pica, G. Rodono, and R. Volpes, "An experimental investigation on natural convection of air in a vertical channel," *Int. J. Heat Mass Transf.*, vol. 36, no. 3, pp. 611–616, 1993. https://doi.org/10.1016/0017-9310(93)80036-T

[2] S. Burek and A. Habeb, "Air flow and thermal efficiency characteristics in solar chimneys and Trombe Walls," *Energy and Buildings*., vol. 39, no. 2, pp. 128–135, 2007. https://doi.org/10.1016/j.enbuild.2006.04.015

[3] D. Ryan, "Experimental Investigation of Buoyancy Driven Natural Convection for Solar Building Applications," PhD Thesis, Glasgow Caledonian Univ., 2008.

[4] Z. Chen, P. Bandopadhayay, J. Halldorsson, C. Byrjalsen, P. Heiselberg, and Y. Li, "An experimental investigation of a solar chimney model with uniform wall heat flux," *Building and Environment* , vol. 38, no. 7, pp. 893–906, 2003. https://doi.org/10.1016/S0360-1323(03)00057-X

[5] M. Aboulnaga, "A roof solar chimney assisted by cooling cavity for natural ventilation in buildings in hot arid climates: an energy conservation approach in Al-Ain city," *Renewable. Energy*, vol. 14, no. 1–4, pp. 357–363, 1998. https://doi.org/10.1016/S0960-1481(98)00090-1

[6] B. Brinkworth, "Estimation of flow and heat transfer for the design of PV cooling ducts," *Solar Energy*, vol. 69, no. 5, pp. 413–420, 2000. https://doi.org/10.1016/S0038-092X(00)00082-7

[7] B. Brinkworth, R. Marshall, and Z. Ibarahim, "A validated model of naturally ventilated PV cladding," *Solar Energy*, vol. 69, no. 1, pp. 67–81, 2000. https://doi.org/10.1016/S0038-092X(99)00076-6

[8] K. Ong, "A mathematical model of a solar chimney," *Renewable Energy*, vol. 28, no. 7, pp. 1047–1060, 2003. https://doi.org/10.1016/S0960-1481(02)00057-5

[9] T. Borgers and H. Akbari, "Free convective turbulent flow within the trombe wall channel," *Solar Energy*, vol. 33, no. 3–4, pp. 253–264, 1984. https://doi.org/10.1016/0038-092X(84)90156-7

[10] B. Jubran, M. Hamdan, and W. Manfalouti, "Modelling free convection in a Trombe wall," *Renewable Energy*, vol. 1, no. 3–4, pp. 351–360, 1991. https://doi.org/10.1016/0960-1481(91)90044-P

[11] G. Gan, "A parametric study of Trombe walls for passive cooling of buildings," *Energy and Buildings*, vol. 27, no. 1, pp. 37–43, 1998. https://doi.org/10.1016/S0378-7788(97)00024-8

[12] G. Gan and S. Riffat, "A numerical study of solar chimney for natural ventilation of buildings with heat recovery," *Applied Thermal Engineering*, vol. 18, no. 12, pp. 1171–1187, 1998. https://doi.org/10.1016/S1359-4311(97)00117-8

[13] B. Zamora and A. Kaiser, "Optimum wall-to-wall spacing in solar chimney shaped channels in natural convection by numerical investigation," *Applied Thermal Engineering*, vol. 29, no. 4, pp. 762–769, 2009. https://doi.org/10.1016/j.applthermaleng.2008.04.010

[14] B. Zamora and A. Kaiser, "Thermal and dynamic optimization of the convective flow in Trombe Wall shaped channels by numerical investigation," *Heat and Mass Transfer*, vol. 45, no. 11, pp. 1393–1407, 2009. https://link.springer.com/article/10.1007/s00231-009-0509-6

[15] B. Zamora and A. Kaiser, "Numerical study on mixed buoyancy-wind driving induced flow in a solar chimney for building ventilation," *Renewable Energy*, vol. 35, no. 9, pp. 2080–2088,2010. https://doi.org/10.1016/j.renene.2010.02.009

[16] B. Zamora and A. S. Kaiser, "Radiative and variable thermophysical properties effects on turbulent convective flows in cavities with thermal passive configuration," *International Journal of Heat and Mass Transfer*, vol. 109, pp. 981–996, 2017. https://doi.org/10.1016/j.ijheatmasstransfer.2017.02.065

[17] B. Zamora, "Morphological comparative assessment of a rooftop solar chimney through numerical modeling," *International Journal of Mechanical Sciences*, vol. 227, 107441, 2022. https://doi.org/10.1016/j.ijmecsci.2022.107441

[18] N. Qasem, B. Imteyaz, R. Ben-Mansour, and M. Habib, "Effect of radiation heat transfer on naturally driven flow through parallel-plate vertical channel," *Arabian Journal for Science and Engineering*, vol. 42, pp. 1817–1829, 2017. https://link.springer.com/article/10.1007/s13369-016-2319-8

[19] T. Yilmaz and S. Fraser, "Turbulent natural convection in a vertical parallel-plate channel with asymmetric heating," *International Journal of Heat and Mass Transfer*, vol. 50, no. 13–14, pp. 2612–2623, 2007. https://doi.org/10.1016/j.ijheatmasstransfer.2006.11.027

[20] T. Yilmaz and A. Gilchrist Temperature and velocity field characteristics of turbulent natural convection in a vertical parallel-plate channel with asymmetric heating. *Heat and mass transfer*.; vol. 43, no. 7: pp. 707-19, 2007. https://link.springer.com/article/10.1007/s00231-007-0234-y

[21] B. Brinkworth and M. Sandberg, "Design procedure for cooling ducts to minimise efficiency loss due to temperature rise in PV arrays," *Solar Energy*, vol. 80, no. 1, pp. 89–103, 2006. https://doi.org/10.1016/j.solener.2005.05.020

[22] Y. Nassar et al., "Thermoelectrical analysis of a new hybrid PV-thermal flat plate solar collector," *8th International Engineering Conference on Renewable Energy &*

Sustainability (ieCRES), 2023, pp. 1–5. https://ieeexplore.ieee.org/document/10209472

[23] J. Liu et al., "Passive photovoltaic cooling: advances toward low ‐ temperature operation," *Advanced Energy Materials*, vol. 14, no. 2, 2302662, 2024. https://doi.org/10.1002/aenm.202302662

[24] B. Prabhu, P. Gurusamy, A. Singh, and T. Arunkumar, "Solar photovoltaic cooling using Paraffin phase change material: Comprehensive assessment," *Renewable and Sustainable Energy Reviews*, vol. 197, 114372, 2024. https://doi.org/10.1016/j.rser.2024.114372

[25] K. Iwabuchi et al., "Enhancing grid stability in PV systems: A novel ramp rate control method utilizing PV-cooling technology," *Applied Energy*, vol. 378, 124737, 2025. https://doi.org/10.1016/j.apenergy.2024.124737

[26] A. Habeb, "Airflow Performance in Close Sided Vertical Channel," Libyan Journal of Contemporary Academic Studies, pp. 280–291, 2025. https://ljcas.ly/index.php/ljcas/article/view/105/112

[27] A. Habeb, "Natural Convection in Closed-Sided Inclined Channels," *African Journal of Advanced Pure and Applied Sciences (AJAPAS)*, pp. 38–54, 2025. https://aaasjournals.com/index.php/ajapas/article/view/1302/1215

[28] CHAM Ltd., "PHOENICS - TR 346, The K-Omega Turbulence Model," https://www.cham.co.uk/phoenics/dpolis/d_enc/turmod/enc_t346.htm, Accessed Apr. 2025.

[29] H. Versteeg and W. Malalasekera, An Introduction to Computational Fluid Dynamics: The Finite Volume Method. Longman, 2007. https://www.pearsoned.co.uk

[30] D. Spalding, "A general purpose computer program for multi-dimensional one-and two-phase flow," *Mathematics and Computers in Simulation*, vol. 23, no. 3, pp. 267–276, 1981. https://doi.org/10.1016/0378-4754(81)90083-5

[31] D. B. Spalding, "Numerical computation of multi-phase fluid flow and heat transfer," *In Von Karman Inst. for Fluid Dynamics*, pp. 161–191, 1981. https://ui.adsabs.harvard.edu/abs/1981ncmp.vkif..161S/abstract

[32] D. Wilcox, "Reassessment of the scale-determining equation for advanced turbulence models," AIAA Journal., vol. 26, no. 11, pp. 1299–1310, 1988. https://doi.org/10.2514/3.10041

[33] D. Wilcox, Turbulence Modeling for CFD, 2nd ed., La Canada, CA: DCW Industries, 1998. http://sutlib2.sut.ac.th/sut_contents/H133907.pdf

[34] S. Patankar, Numerical Heat Transfer and Fluid Flow. CRC Press, 2018. https://doi.org/10.1201/9781482234213

[35] M. Miyamoto, Y. Katoh, J. Kurima, and H. Sasaki, "Turbulent free convection heat transfer from vertical parallel plates," in Heat Transfer, vol. 4, C. L. Tien, V. P. Carey, and J. K. Ferrell, Eds., Hemisphere, pp. 1593–1598, 1986. https://cir.nii.ac.jp/crid/1870583642988357632

[36] A. Bouchair, "Solar chimney for promoting cooling ventilation in southern Algeria," Building Services Engineering Research and Technology, vol. 15, no. 2, pp. 81–93,1994. https://journals.sagepub.com/doi/abs/10.1177/014362449401500203

[37] E. Sparrow and J. Gregg, "Laminar free convection from a vertical plate with uniform surface heat flux," *Transactions of the American Society of Mechanical Engineers*, vol. 78, no. 2, pp. 435–440, 1956. https://doi.org/10.1115/1.4013697

[38] L. Azevedo and E. parrow, "Natural convection in open-ended inclined channels," *Int. J. Heat Mass Transfer*, pp. 893–901, 1985. https://doi.org/10.1115/1.3247518

[39] M. Sandberg and B. Moshfegh, "Buoyancy-induced air flow in photovoltaic facades: Effect of geometry of the air gap and location of solar cell modules," *Building and Environment*, vol. 37, no. 3, pp. 211–218, 2002. https://doi.org/10.1016/S0360-1323(01)00025-7

[40] J. Holman, Heat Transfer, McGraw-Hill, USA, 2010.

Appendix 1

An UQ (Uncertainty Quantification) analysis was conducted to increase the reliability of the CFD results and to address uncertainties such as variation of the input values, discretization errors, and assumption errors regarding the model figure. For estimating the numerical uncertainty regarding grid resolution, a GCI (Grid Convergence Index) assessment was done. Numerical simulations were done on three structured grids at different refinement levels (coarse, medium, and fine). All quantity values were monitored. Using the ASME methodology for estimating GCI, both the observed convergence behavior and refinement ratios were computed. A safety factor of 1.25 was introduced in this calculation. For the finest grid, GCI was reported lower than 2.5%, which indicates good convergence. Boundary conditions, including heat input, emissivity, and boundary temperatures, were set with uncertainties of ±5%, which is expected to cause about ±4% change in Nusselt number and Reynolds number both. Due to the turbulence model k–ω, the resultant modeling error is expected to be at least 5%, which is proportional to the natural convection modeling error. The error on the mass flow rate ($\dot{m}$) is ±7% and arises from both input variability and the modeling method. These values reflect relatively good confidence in the simulation results, and as such, support the degree to which the correlations provided can be used. The model is two-dimensional and uses the k–ω turbulence model; radiation modeling is not included. Even if a simple radiation modeling has been activated with the Imersol radiation model, no complete radiation coupling was achieved. Such an approximation might introduce small errors, especially in the temperature distribution close to the walls. The results still show reasonable agreement with experimental literature and remain within the appropriate uncertainty bounds.